Acta Materialia 281 (2024) 120435

Contents lists available at ScienceDirect

Acta Materialia

journal homepage: www.elsevier.com/locate/actamat

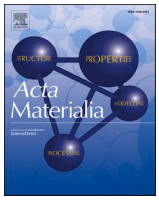

Rotational deformation twins in a HfNbTaTiZr refractory high entropy alloy

Oleg N. Senkov [a,b,*], Frederick Meisenkothen [c], Robert Wheeler [a,d]

[a] Air Force Research Laboratory, Materials and Manufacturing Directorate, Wright-Patterson AFB, OH 45433, United States
[b] MRL Materials Resources LLC, Xenia Township, OH 45385, United States
[c] National Institute of Standards and Technology, Gaithersburg, MD 20899, United States
[d] UES, Inc., Dayton, OH 45432, United States

ARTICLE INFO

Keywords:
Refractory alloy
Refractory high entropy alloy
HfNbTaTiZr
Microstructure
Deformation twinning

ABSTRACT

Results of the analysis of deformation twins formed in a HfNbTaTiZr refractory high entropy alloy during compression deformation at 20 °C – 600 °C are reported. All studied twins were formed by rotation of the matrix crystal lattice around a ⟨110⟩ pole and have the common reciprocal twinning plane K_2 = {001} and reciprocal twinning direction η_2 = <1$\bar{1}$0>. At the same time, the twinning plane K_1 and direction η_1 depend on the degree of rotation of K_2 and η_2 around the common ⟨110⟩ pole. The following rotational twinning modes have been identified in HfNbTaTiZr: {1$\bar{1}$4}<2$\bar{2}$1> (38.94° rotation), {1$\bar{1}$5}<5$\bar{5}$2> (31.58°), {1$\bar{1}$6}<3$\bar{3}$1> (26.54°), {1$\bar{1}$7}<7$\bar{7}$2> (22.84°), and {1$\bar{1}$8}<4$\bar{4}$1> (20.04°). A rotational mechanism of twinning, with the rotation axis ⟨011⟩ or ⟨001⟩, is proposed as an alternative to the commonly accepted shear mechanism.

1. Introduction

An equiatomic HfNbTaTiZr refractory high entropy alloy (RHEA), which is also called the Senkov alloy [1], is currently one of the most studied refractory high entropy alloys (RHEAs) because of its unique mechanical properties and processability [2-5]. In particular, it has high strength, good strain hardening behavior, excellent malleability and good tensile ductility in a wide temperature range. Despite its body centered cubic (BCC) crystal structure, the Senkov alloy does not have a ductile-to-brittle transition temperature at or above -196 °C [6]. In fact, the alloy can easily be cold rolled or forged to very high strains, both at room temperature and cryogenic temperatures [4,5,7-11]. Thermo-mechanical processing consisting of cold working and recrystallization annealing has been used to refine the microstructure and control strength and ductility of the Senkov alloy [5,12,13].

Detailed microstructural analysis aided with solid solution strengthening models indicates that the yield strength of this alloy at room temperature is mainly controlled by the mobility of screw dislocations [14,15]. At later stages of deformation, heterogeneous microstructures consisting of slip bands, deformation twins, kink bands and shear bands were reported [2-5,16,17]. Deformation twins in HfNbTaTiZr were first reported by Senkov et al. [2,3] after 50 % compression deformation at 23 °C, 400 °C and 600 °C; however, the type of twins was not described. Cizek et al. [18] observed {113}<332> twins during early stages of high pressure torsion processing. The twinning mechanism occurred predominantly in grains with orientations unfavorable for shear in {110}<111> and {112}<111> slip systems. Wang et al. [19] reported very good tensile ductility of the Senkov alloy at -196 °C and related this to the activation of {112}<111> nano-twinning accompanied by formation of hexagonal omega-phase nano-particles and extensive dislocation slip. Zherebtsov, et al. [7] studied the alloy microstructure after room-temperature (RT) rolling to different levels of the plate thickness reduction, up to 80 %. After rolling with 15 % to 40 % thickness reduction, they observed features similar to deformation twins but interpreted them as kink bands, because the misorientation angles between the matrix grain and the bands were not constant along the interfaces. Characteristic misorientation angles were reported to be 20° or smaller after 15 % rolling and approximately 30° - 50° after 40 % rolling.

In the present work, we report deformation twins of different types observed in the Senkov alloy after compression deformation at room temperature (RT, ~22–27 °C), 400 °C and 600 °C. All the observed twins have a common ⟨110⟩ pole with the parent grain and form by rotation of the grain segment to a fixed angle about this pole. Contrary to deformation kinks, which also form by crystal rotation about a ⟨110⟩ pole and whose formation is associated with the cooperative dislocation glide in {112}<1$\bar{1}$1> slip systems [20], the observed twins likely form by localized cooperative shear in {110}<001> systems and follow twin

* Corresponding author.
E-mail address: oleg.senkov.ctr@afrl.af.mil (O.N. Senkov).

https://doi.org/10.1016/j.actamat.2024.120435
Received 26 July 2024; Received in revised form 16 September 2024; Accepted 25 September 2024
Available online 26 September 2024

symmetry operations.

2. Experimental procedures

The Senkov alloy was prepared by vacuum arc melting of an equimolar mixture of the corresponding elements. The prepared button was about 10 mm in thickness and 50 mm in diameter. To heal internal cast porosity and other defects, the button was hot isostatically pressed at 1200 °C and 207 MPa for 1 h, then vacuum annealed at 1200 °C for 24 h and slow cooled inside the furnace after turning the power off. Details of the alloy preparation are given elsewhere [3]. The alloy composition, determined with the use of inductively coupled plasma-optical emission spectroscopy (ICP-OES), is given in Table 1.

Compression tests were conducted at RT, 400 °C and 600 °C using cylindrical specimens of 3.8 mm in diameter and 6.1 mm in height, which were extracted from a middle section of the annealed alloy button. The specimen axis was perpendicular to the bottom button surface, which was in contact with the water-cooled copper hearth during arc melting and solidification. The specimen surfaces were mechanically polished, and the compression faces of the specimens were paralleled. A computer-controlled Instron[e] (Instron, Norwood, MA) mechanical testing machine outfitted with a Brew vacuum furnace and silicon carbide dies was used. The elevated temperature tests were conducted in a vacuum of 10^{-3} Pa or better. The specimens were heated to each testing temperature at a heating rate of 20 °C/min, soaked at the temperature for 15 min and then deformed to a true plastic strain of 0.4 at the strain rate of 10^{-3} s^{-1}. Room temperature tests were conducted in air using the same deformation conditions.

The microstructure was analyzed with the use of scanning electron microscopes (SEM) FEI Quanta 650F FEG SEM, equipped with an EDAX Hikari electron backscatter diffraction (EBSD) detector and TSL OIM data acquisition system, and Thermo Fisher Scientific Apreo C FEG SEM, integrated with an Oxford Instruments Symmetry EBSD detector and AZtec data acquisition system. Quantitative analysis of twins was conducted using AZtec Crystal v.6.0 software.

3. Classification of deformation twins and kinks

In the materials science literature, deformation twins are mostly considered as type I twins formed by a simple shear of the crystal lattice in a specific plane K_1, called the twinning or composition plane, along a specific shear direction η_1 [21-26]. The type I twinning mechanism by shear is summarized in Fig. 1 showing displacement of a circle to an ellipse by a shear vector ***s*** at a unit distance above the origin. The shear plane K_1 and shear direction η_1 remain undistorted during this type of twinning. The second undistorted (but rotated by the angle 2ϕ) plane of the simple shear (also called a reciprocal twinning plane) is denoted by K_2, and the plane perpendicular to K_1 and K_2 by P (plane of shear). A reciprocal twinning direction η_2 is defined as a vector, which resides in both K_2 and P planes (Fig. 1). For the type I twinning mode, K_1 and η_2 must have rational indices, while K_2 and η_1 can have irrational (general case) or rational (compound twin mode) indices. In BCC cubic crystals, a common example of shear twinning is the simple shear of {112} planes in a $<11\bar{1}>$ direction, however; other types of shear twinning such as $\{113\}<33\bar{2}>$ and $\{114\}<22\bar{1}>$ have also been reported [18,27,28].

Table 1
Chemical composition (in at.%) of the produced HfNbTaTiZr.

Element	Hf	Nb	Ta	Ti	Zr
Composition, at. %	20.5 ± 0.6	18.9 ± 0.6	19.7 ± 0.6	19.7 ± 0.6	21.2 ± 0.6

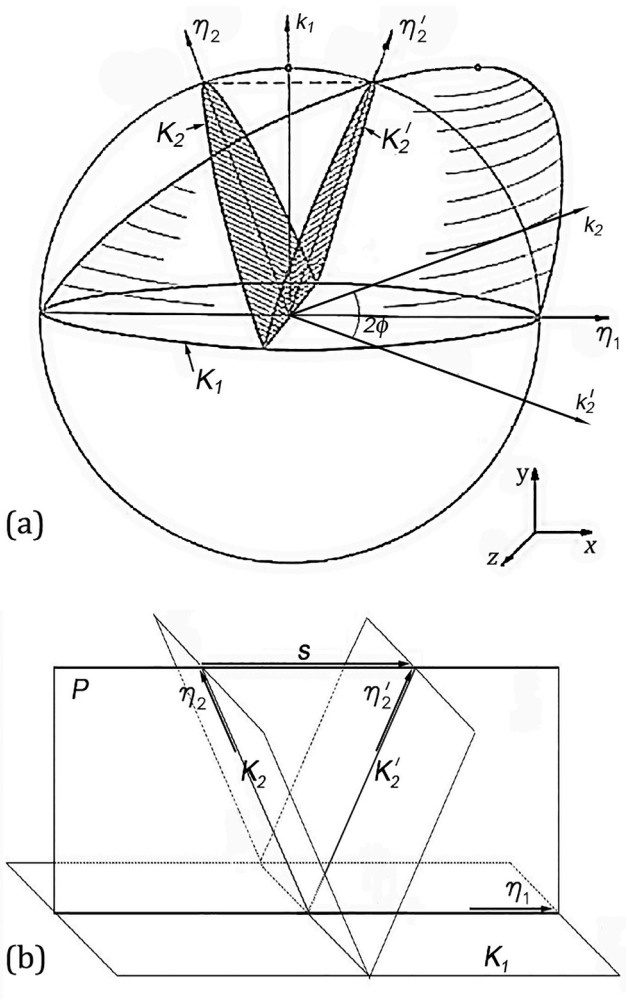

Fig. 1. (a) Relation of the matrix sphere and twinned ellipsoid. (b) Illustration of twinning elements: P is plane of shear, K_1 – twinning plane, η_1 – twinning direction, K_2 and K_2' conjugate (or reciprocal) twinning plane before and after shear, η_2 and η_2' – conjugate (or reciprocal) twinning direction before and after shear and s is the shear vector, which is parallel to η_1. Vectors k_1, k_2 and k_2' are normals to the respective planes. The shear angle (between K_2 and K_2') is 2ϕ.

During type II twinning, shear occurs on K_2 planes and accumulates in tilt walls (twin boundaries). This mechanism is accompanied by partitioning of the rotations to both the matrix and twin, creating symmetrical tilt across the twin boundary [26,29,30]. This means that the type II twinning involves both crystal shear and rotation. For the type II twinning mode, K_2 and η_1 have rational indices and K_1 and η_2 are generally irrational. In BCC crystals, all four twinning elements can have rational indices.

The commonly observed symmetry relations between twin and matrix are reflection across the twinning plane K_1, rotation of 180° about twinning direction η_1, reflection in the plane normal to η_1, and rotation of 180° about the normal to K_1 [22,23,25].

In addition to, or instead of twinning, deformation kink bands may form in grains oriented unfavorably for dislocation slip. Under tension or compression stress, the grain sharply bends (kinks) towards increasing the Schmid factor of a slip system inside the bend and deformation localizes into the kink band [20,31]. The crystal rotation during bending

[e] Disclaimer: Certain commercial equipment, instruments, or materials are identified in this paper in order to specify the experimental procedure adequately. Such identification is not intended to imply recommendation or endorsement by the United Stated Air Force or by the National Institute of Standards and Technology, nor is it intended to imply that the materials or equipment identified are necessarily the best available for the purpose.

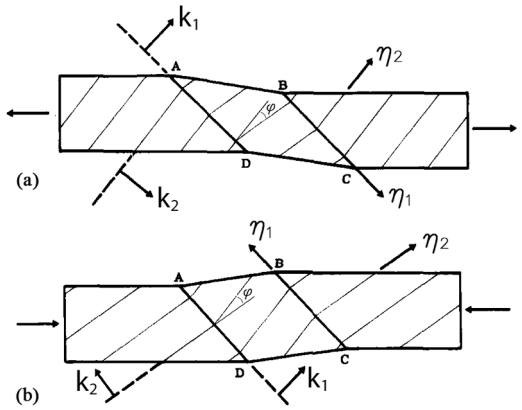

Fig. 2. Schematic illustration of formation of deformation kinks in (a) tension and (b) compression. In each case, a kink ABCD forms following slip on the plane K_2 in the direction η_2. The associated macroscopic deformation can formally be described as a homogeneous shear on the plane K_1 in the direction η_1.

occurs about an axis that lies in the slip plane and perpendicular to the slip direction. In a BCC structure, where slip occurs along a ⟨111⟩ direction within $\{1\bar{1}0\}$, $\{11\bar{2}\}$, $\{12\bar{3}\}$ or $\{13\bar{4}\}$ slip planes, the respective crystal rotation takes place about $\langle 11\bar{2}\rangle$, $\langle \bar{1}10\rangle$, $\langle \bar{5}41\rangle$ or $\langle \bar{7}52\rangle$ directions. Schematic illustration of formation of deformation kinks is given in Fig. 2 (adapted from ref. [20]), where the conventional notation of deformation twinning is used [22,23]. A kink forms following slip on the plane K_2 in the direction η_2. Due to localized slip plane rotation, slip becomes concentrated in region ABCD. Boundaries AD and BD orient themselves symmetrically with respect to the grain and the kink. The associated macroscopic deformation can formally be described as a simple shear on the plane K_1 in the direction η_1 and thus the kink band can form in the same way as a Type II deformation twin. However, contrary to twinning, the shear for the kink band is not restricted to a particular value, but increases uniformly as the plastic strain increases.

4. Results

4.1. Deformation behavior

True stress vs true strain compression curves of HfNbTaTiZr at RT, 400 °C and 600 °C are shown in Fig. 3. The alloy had yield stress of 925 MPa, 790 MPa and 675 MPa, respectively, at these temperatures. After yielding, continuous strain hardening was observed, which slowed down with an increase in strain. Starting from about 0.12 true strain, serrated behavior of flow stress was observed at RT and 400 °C. At 600 °C, the serrated behavior started after the true strain of about 0.3. After deformation to a true strain of 0.4, the true stress of the alloy increased to 1410 MPa, 1365 MPa and 1250 MPa, respectively, at RT, 400 °C and 600 °C.

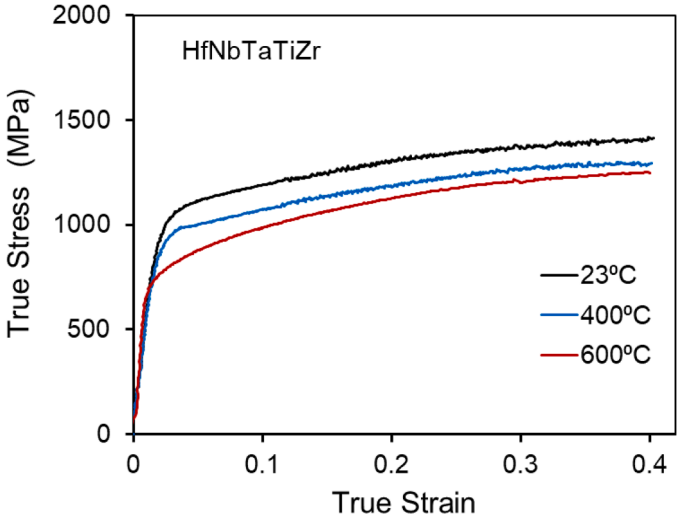

Fig. 3. True stress versus true strain deformation curves of HfNbTaTiZr at RT (23 °C), 400 °C and 600 °C.

4.2. Deformation twinning

The microstructure of the Senkov alloy in the annealed condition and after compression deformation at different temperatures was described in details in earlier publications [2,3]. Formation of twins during the deformation at RT, 400 °C and 600 °C was also reported there; however, the types of the twins were not studied at that time. In the following sections, the results of a detailed analysis of these twins are reported and a rotational nature of these twins is revealed.

4.2.1. Deformation twinning at room temperature

Fig. 4 represents the microstructure of the Senkov alloy after 0.4 true strain at room temperature. Many grains are twinned (Fig. 4a), the Kernel average misorientation map indicates an increased dislocation density near grain and twin boundaries (Fig. 4b), and the Schmid factor distribution map shows activation of {112}<111> (23.7 %), {110}<111> (13.8 %) and {123}<111> (45.9 %) slip systems (Fig. 4c). It can be noted that the {112}<111> and {123}<111> slip systems dominate inside grains while the {110}<111> slip system mainly operates inside the twins. The misorientation angle distribution map shows several distinct maxima for the neighbor grain misorientations, in particular near 20°, 26.5°, 30° and 60° (Fig. 4d). The 60° misorientation corresponds to conventional, $\{112\}\langle\bar{1}\bar{1}1\rangle$ type twins, while 20.04°, 26.53° and 31.58° misorientations are found to correspond to $\{118\}\langle 44\bar{1}\rangle$, $\{116\}\langle 33\bar{1}\rangle$ and $\{115\}\langle 55\bar{2}\rangle$ type twins (as illustrated below).

Fig. 5a shows a magnified twinned grain area outlined by a red rectangle in Fig. 4a. The {011} pole figure from the grain containing twins reveals that the twins and the parent grain have a common $[\bar{1}01]$ pole, outlined by a red circle (Fig. 5a insert). To verify if this common pole represents the normal direction to the plane of shear, P, we rotate the sample in such a way that the common $[\bar{1}01]$ pole becomes parallel to the normal (Z) direction (Fig. 5b insert). After such sample rotation, the IPF color of the grain and the twins on the IPF map becomes the same (green), which confirms that the grain and twins now have the same crystallographic orientation $[\bar{1}01]$ in the Z direction (Fig. 5b), and the mirror symmetry between the ⟨110⟩ poles from the grain and twins is revealed (Fig. 5b insert).

If $(\bar{1}01)$ is the plane of shear, then all the twinning elements (vectors η_1, η_2, η_2', k_1, k_2 and k_2', see Fig. 1) on the stereographic projections with the pole $[\bar{1}01]$ in the center (0°, parallel to the normal (Z) direction) should be located on the 90° great circle (i.e. inside the $(\bar{1}01)$ plane). The discrete pole figures, Fig. 6, from the twins #1 and #2 (Fig. 5b) and the parent grain show that the poles [010], [101], [111], $[1\bar{1}1]$, [121] and $[12\bar{1}]$, from both the twins and the parent grain, are in the plane $(\bar{1}01)$ and the angle between the grain and the twin poles with the same indexes is the same, ≈ 20.05°, i.e. the twin's crystal lattice is rotated by 20.05° about the $[\bar{1}01]$ direction relative to the parent grain lattice. There are also two orthogonal poles in the plane $(\bar{1}01)$, which are common to the matrix and twins. From Fig. 6, these are experimentally determined $[\bar{1}8\bar{1}]_M \,||\, [181]_T$ and $[414]_M \,||\, [4\bar{1}4]_T$. The subscripts 'M' and 'T' indicate that the indices belong to the matrix grain and twin, respectively. The traces of the respective $(\bar{1}8\bar{1})_M \,||\, (181)_T$ and $(414)_M \,||\, (4\bar{1}4)_T$ planes are shown as red dashed lines on the pole figures. Inspection of the pole figures indicates that the poles of the twins can be derived from the poles of the matrix by reflection in these two

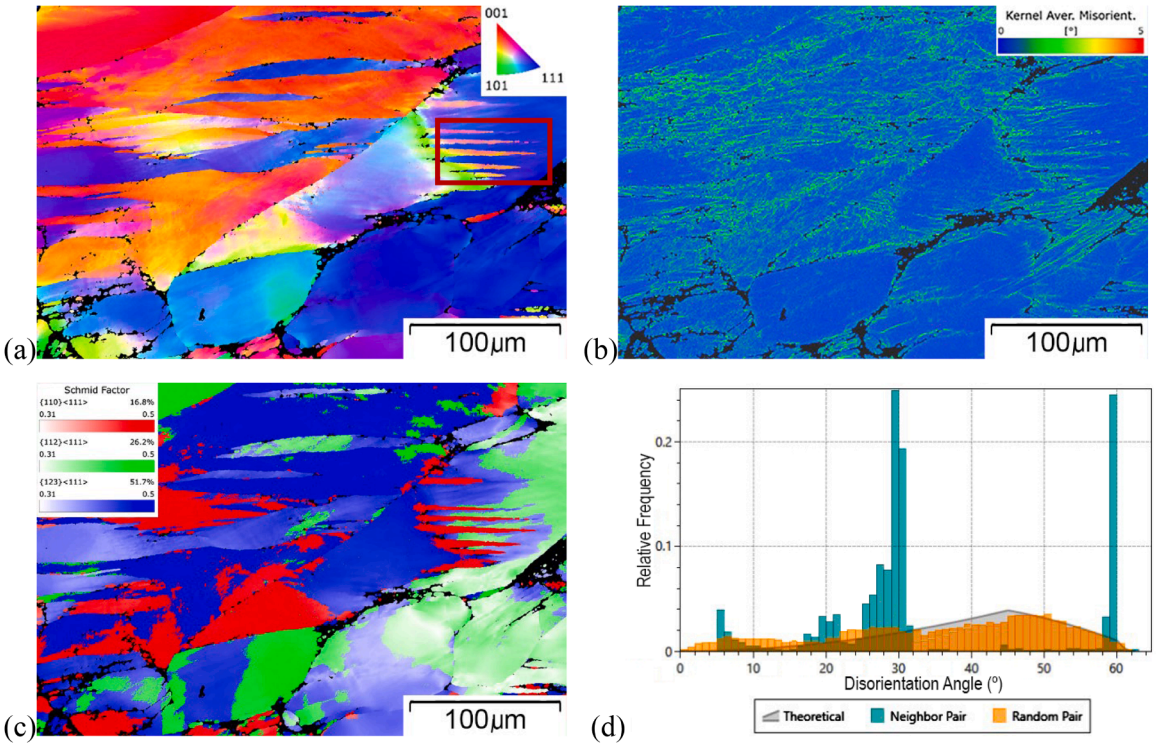

Fig. 4. HfNbTaTiZr after RT compression deformation: (a) Inverse pole figure (IPF) map of grain orientations in compression (vertical, Y) direction, (b) Kernel average misorientation distribution map, (c) Schmid factor distribution map in compression direction and (d) Neighbor pair (green) and random pair (orange) misorientation angle distribution.

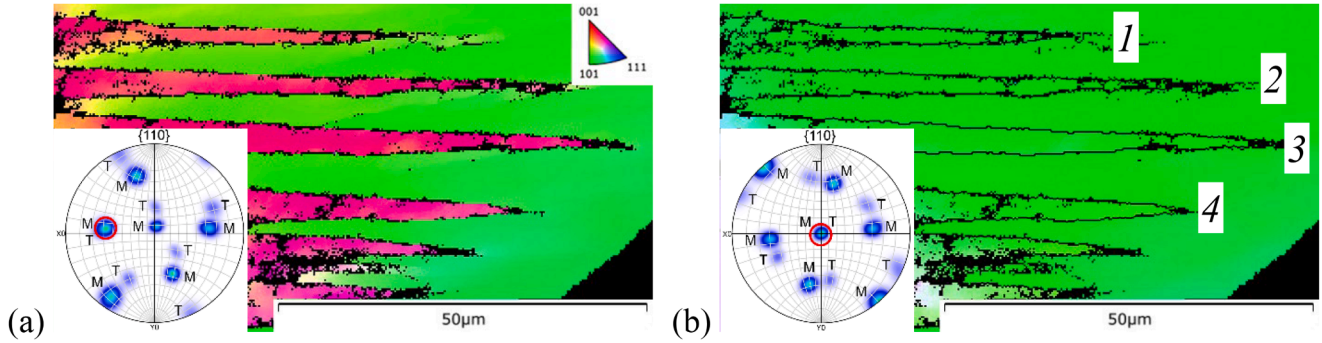

Fig. 5. Magnified IPF maps of grain and twin orientations in normal (Z) direction, from the area inside the red box in Fig. 4a, and the respective ⟨110⟩ pole figures (a) in an original sample position and (b) after the sample rotation to orient the [$\bar{1}$01] crystal direction, common to the twins and the parent grain, parallel to the Z direction. The common [$\bar{1}$01] pole is outlined by the red circle in the ⟨110⟩ pole figures. The matrix-grain poles are identified by the letter M and the poles belonging to the twins are identified by the letter T.

orthogonal planes. Therefore, by definition, one of these planes $(\bar{1}8\bar{1})_M$ || $(181)_T$ is the composition plane K_1 and the normal to the other plane, $[414]_M$ || $[4\bar{1}4]_T$, is the shear direction η_1 [21]. The grain to twin transformation is completely described by the rotational transformation matrix:

$$A_{(1\bar{8}\bar{1})(414)} = \frac{1}{33}\begin{vmatrix} 32 & \bar{8} & \bar{1} \\ 8 & 31 & 8 \\ \bar{1} & \bar{8} & 32 \end{vmatrix} \quad (1)$$

Using the similar approach, twins 3 and 4 in Fig. 5b are identified as {1$\bar{6}$1}<313> type twins formed by 26.53° rotation about [$\bar{1}$01] (Fig. 7) and for which the transformation matrix is:

$$A_{(1\bar{6}\bar{1})(313)} = \frac{1}{19}\begin{vmatrix} 18 & \bar{6} & \bar{1} \\ 6 & 17 & 6 \\ \bar{1} & \bar{6} & 18 \end{vmatrix} \quad (2)$$

Fig. 8a shows the other grain with a set of twins in the HfNbTaTiZr sample deformed at RT. The twins and the grain have a common [011] orientation in Z direction and thus the twins are not seen on the Z IPF map (Fig. 8b). The analysis of the pole figures from the grain and the twins reveals that these twins were formed by 31.58° clockwise crystal rotation around the [011] pole (Fig. 8c). The matrix and twin poles have a mirror symmetry about the $(5\bar{1}1)_M$ || $(51\bar{1})_T$ and $(\bar{2}55)_M$ || $(2\bar{5}5)_T$ composition planes (Fig. 8c). The twinning elements have been identified as $K_2 = (01\bar{1})$, $\eta_2 = [100]$, $K_1 = (5\bar{1}1)$ and $\eta_1 = [\bar{2}\bar{5}5]$. The grain to twin orientation relationship is described by the following transformation matrix:

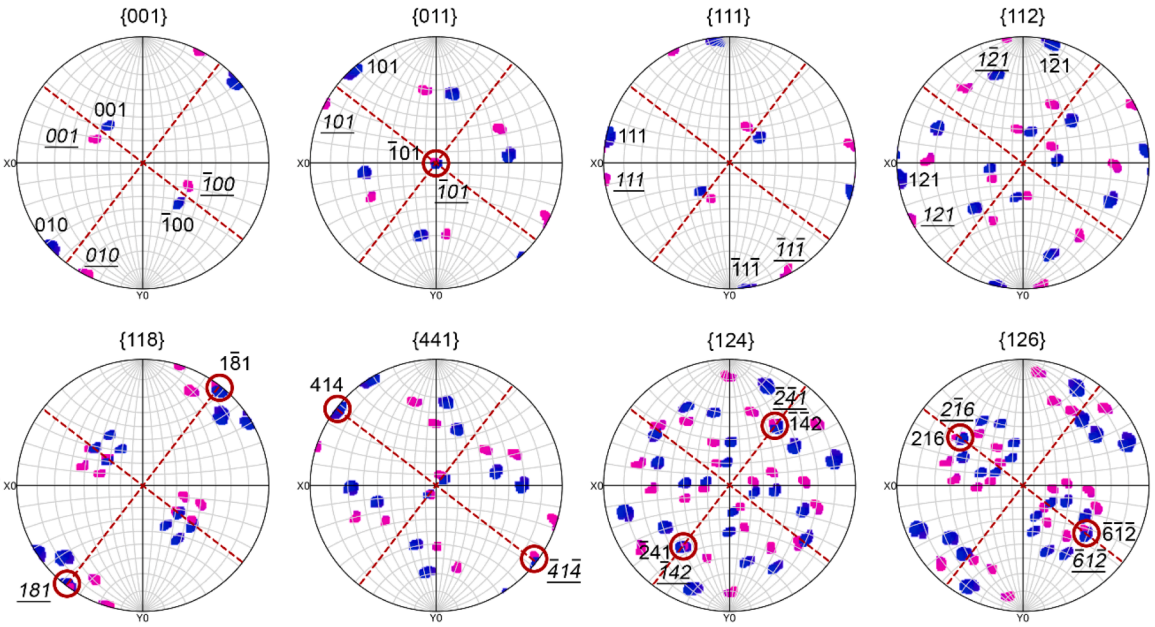

Fig. 6. Discrete (scattered) pole figures from twins #1 and #2 (red spots) shown in Figure 5b and the parent grain (blue spots). Both twins have the same crystallographic orientation. The poles, which are common to the twins and the grain, are outlined by red circles. Indexes from the representative twin poles are underlined. Two orthogonal dashed lines crossing the centers of the stereographic projections represent the traces of the $(\bar{1}8\bar{1})_M$ || $(181)_T$ and $(414)_M$ || $(4\bar{1}4)_T$ composition (mirror) planes. The twinning elements are: $P = (\bar{1}01)$, $K_2 = (\mathbf{101})$, $\eta_2 = [\mathbf{010}]$, $K_1 = (1\bar{8}1)$, $\eta_1 = [\mathbf{414}]$, $2\phi = 20.05°$ and $s = 0.354$.

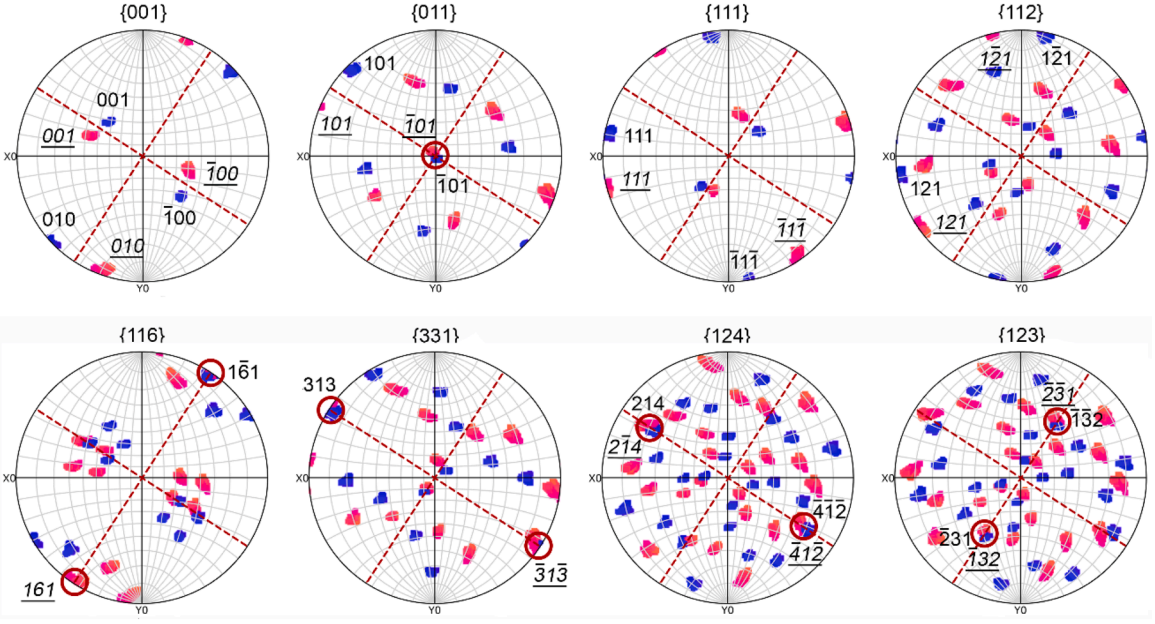

Fig. 7. Discrete (scattered) pole figures from twins #3 and #4 shown in Figure 5b (red spots) and the parent grain (blue spots). The poles, which are common to the twin and the grain, are outlined by red circles. Indexes from the representative twin poles are underlined. Two orthogonal dashed lines crossing the centers of the stereographic projections represent the traces of the $(\bar{1}6\bar{1})_M$ || $(1\mathbf{6}1)_T$ and $(313)_M$ || $(3\bar{1}3)_T$ composition (mirror) planes. The twinning elements are: $P = (\bar{1}01)$, $K_2 = (\bar{1}0\bar{1})$, $\eta_2 = [\mathbf{010}]$, $K_1 = (1\bar{6}1)$, $\eta_1 = [\mathbf{313}]$, $2\phi = 26.53°$ and $s = 0.471$.

$$A_{(5\bar{1}1)(\bar{2}\bar{5}5)} = \frac{1}{27}\begin{vmatrix} 23 & 10 & \bar{10} \\ \bar{10} & 25 & 2 \\ 10 & 2 & 25 \end{vmatrix} \quad (3)$$

4.2.2. Deformation twinning at 400 °C

Fig. 9 illustrates deformed grains in HfNbTaTiZr after 0.4 true strain at 400 °C. Deformation twins and kinks are seen inside the grains (Fig. 9a,b), The Kernel average misorientation map indicates an increased dislocation density near grain and interface boundaries, as well as inside the rotated regions (Fig. 9c). The disorientation angle distribution map shows distinct maxima near 23° and 31°, as well as a small maximum near 51°, for the neighbor pixel pair misorientations (Fig. 9d), which correspond to $\{\bar{1}17\}\langle 7\bar{7}2\rangle$ (2ϕ=22.84°), $\{\bar{1}15\}\langle 5\bar{5}2\rangle$ (2ϕ=31.58°) and $\{\bar{1}13\}\langle 3\bar{3}2\rangle$ (2ϕ=50.4°) type twins. There is also a wide neighbor-pair misorientation distribution in the 2ϕ range between 10° and 20°, which is likely characteristic of deformation kink bands. (See also Section 1 of Supplementary Materials for additional details.)

Fig. 10a shows a magnified twinned grain area outlined by a

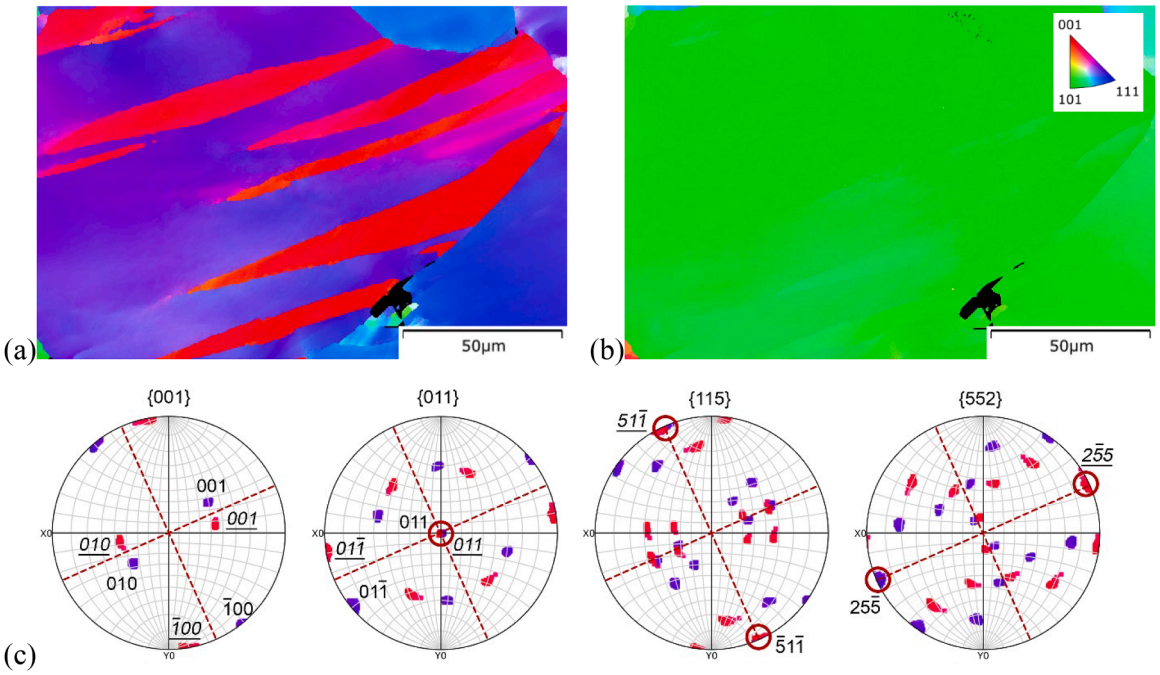

Fig. 8. (a,b) IPF orientation maps of twins and the parent grain in (a) vertical (Y) direction and (b) normal (Z) direction. The IPF color code is shown at the top right corner of figure (b). (c) Discrete (scattered) pole figures from the twins shown in (a) (red spots) and the parent grain (blue spots). The poles, which are common to the twins and the grain, are outlined by red circles. Indexes from the representative twin poles are italicized and underlined. Two orthogonal dashed lines crossing the centers of the stereographic projections represent the traces of the $(5\bar{1}1)_M$ || $(51\bar{1})_T$ and $(25\bar{5})_M$ || $(\bar{2}5\bar{5})_T$ composition (mirror) planes. The twinning elements are: $P = (011)$, $K_2 = (01\bar{1})$, $\eta_2 = [100]$, $K_1 = (5\bar{1}1)$, $\eta_1 = [\bar{2}55]$, $2\phi = 31.58^\circ$ and $s = 0.566$.

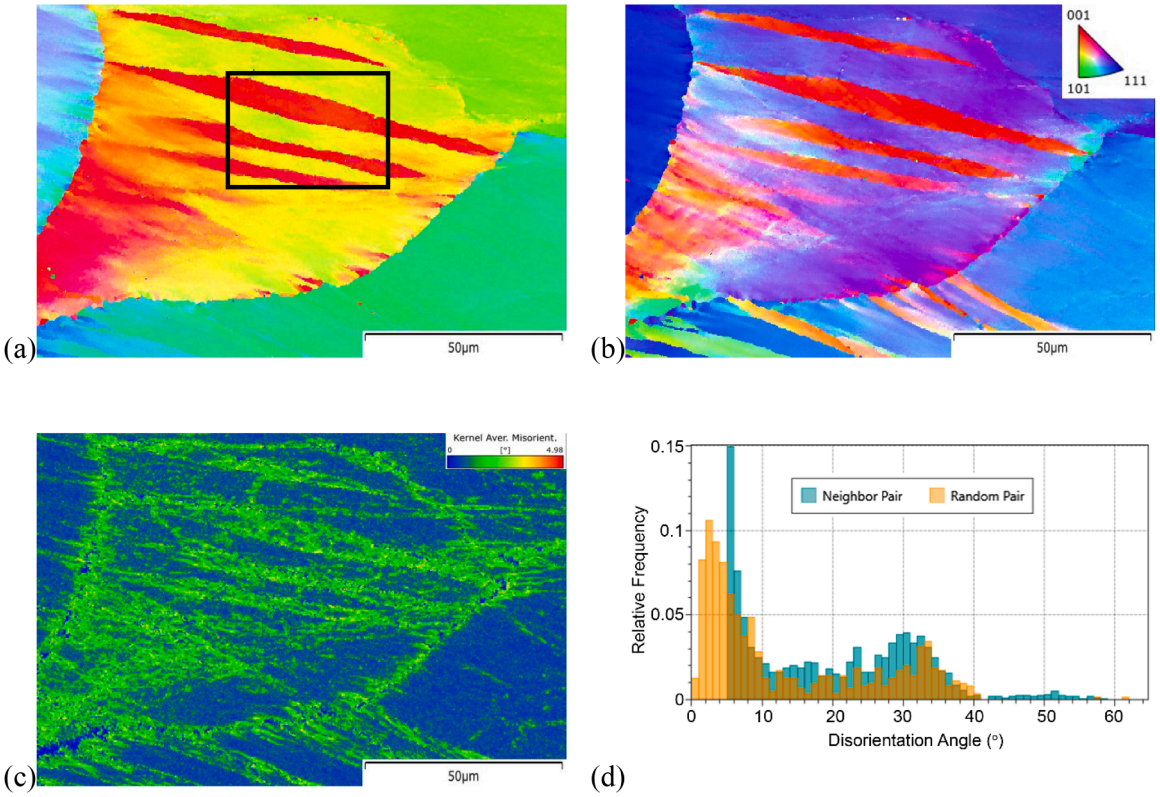

Fig. 9. (a, b) IPF maps of grains and twins in (a) normal (Z) and vertical (Y) directions, (c) Kernel average misorientation map and (d) disorientation angle distributions between neighbor pixel pairs (blue) and random pixel pairs (orange). The compression direction is vertical.

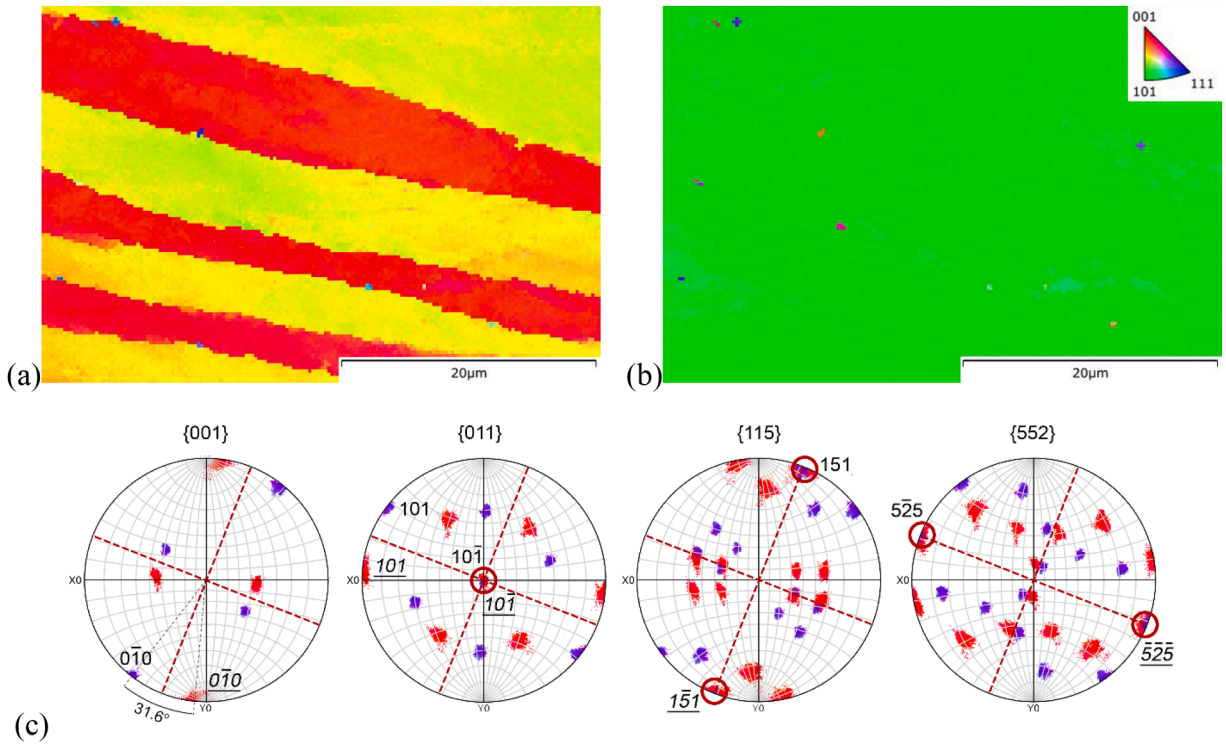

Fig. 10. (a,b) IPF maps of the selected twins and the parent grain in (a) original sample position and (b) after rotating the sample and positioning the common $[10\bar{1}]$ pole parallel to Z direction. The color coded IPF is shown on the top of figure (b). (c) Scattered-orientation pole figures from the studied region, with $[10\bar{1}]$ parallel to Z. Two orthogonal dashed lines crossing the centers of the stereographic projections represent the traces of the $(151)_M$ || $(\bar{1}5\bar{1})_T$ and $(5\bar{2}5)_M$ || $(525)_T$ composition (mirror) planes. The poles from the twins are red and their indexes are underlined, and the poles from the parent grain are blue. The twinning elements are: $P = (10\bar{1})$, $K_2 = (\bar{1}0\bar{1})$, $\eta_2 = [0\bar{1}0]$, $K_1 = (151)$, $\eta_1 = [5\bar{2}5]$, $2\phi = 31.58^\circ$ and $s = 0.566$. HfNbTaTiZr sample after compression deformation at 400 °C.

rectangle in Fig. 9a. The twins have a red IPF color indicating that one of their ⟨001⟩ directions is parallel to the Z direction. The analysis of the pole figures indicates that the twins and the grain have a common $[10\bar{1}]$ pole and other twin poles experience ~31.6° counterclockwise rotation about the $[10\bar{1}]$ pole relative to the respective crystallographic poles of the parent grain. Bringing the common $[10\bar{1}]$ pole to the center of the stereographic projection (i.e. parallel to Z direction) results in the same (green) IPF color of the grain and the twins (Fig. 10b), confirming the same crystallographic orientation of these constituents in Z direction after the respective sample rotation.

Scattered-orientation pole figures from the selected twins and the parent grain after bringing the common $[10\bar{1}]$ pole to the center of the stereographic projection are shown in Fig. 10c. The poles from the grain are blue and those from the twins are red. The pole spots are rather wide, which indicates crystallographic orientation spread, both inside the grain and twins. This was likely due to continuous deformation after the twin formation. Two composition planes, $(151)_M$ || $(\bar{1}5\bar{1})_T$ and $(5\bar{2}5)_M$ || $(525)_T$, providing the mirror symmetry between the twin and parent grain crystallographic orientations, are clearly identified on the pole figures. The twinning elements have been identified as $P = (10\bar{1})$, $K_2 = (\bar{1}0\bar{1})$, $\eta_2 = [0\bar{1}0]$, $K_1 = (151)$ and $\eta_1 = [5\bar{2}5]$. The grain-twin transformation is described by the transformation matrix:

$$A_{(151)[5\bar{2}5]} = \frac{1}{27}\begin{vmatrix} 25 & 10 & \bar{2} \\ \bar{10} & 23 & \bar{10} \\ \bar{2} & 10 & 25 \end{vmatrix} \quad (4)$$

4.2.3. Deformation twinning at 600 °C

Fig. 11a and Fig. 11b show IPF maps, in the vertical (Y) and normal (Z) directions, respectively, of deformation twins and the parent grain after 0.4 true plastic strain at 600 °C. The microstructure of a larger sample area is given in Section 2 of Supplementary Materials. Scattered-orientation pole figures from the grain and twins are shown in Fig. 11c. The twins have a [001] orientation and the grain has an approximate $[\bar{2}23]$ orientation in Y direction, and they all have a common [110] orientation in Z direction. The crystal lattice of the twins is rotated clockwise by 44.0° about [110] relative to the grain crystal lattice. A mirror symmetry of the twin and grain poles relative to two orthogonal crystallographic planes, $(\bar{2}27)_M$ || $(2\bar{2}7)_T$ and $(7\bar{7}4)_M$ || $(7\bar{7}\bar{4})_T$, is clearly identified. The traces of these composition planes are shown as dashed lines crossing the centers of the stereographic projections (Fig. 11c). Based on this analysis, the twinning elements have been identified as $P = (110)$, $K_2 = (\bar{1}10)$, $\eta_2 = [00\bar{1}]$, $K_1 = (2\bar{2}\bar{7})$, $\eta_1 = [\bar{7}\bar{7}\bar{4}]$. The grain to twin transformation is described by the transformation matrix:

$$A_{(2\bar{2}\bar{7})[\bar{7}\bar{7}\bar{4}]} = \frac{1}{57}\begin{vmatrix} 49 & 8 & \overline{28} \\ 8 & 49 & 28 \\ 28 & \overline{28} & 41 \end{vmatrix} \quad (5)$$

5. Discussion

Different types of the deformation twins reported in this work for the Senkov alloy after compression deformation at RT, 400 °C and 600 °C are summarized in Table 2. They all have the reciprocal twin plane $K_2 = \{1\bar{1}0\}$ and the reciprocal twin direction $\eta_2 = \langle 001 \rangle$. Their relationship to the parent grain can be interpreted as rotation to a fixed angle 2ϕ about a ⟨110⟩ axis that lies in K_2 and is perpendicular to η_2. The composition (mirror) plane, K_1 is then identified as the plane containing the rotation axis ⟨110⟩ and having the angle of $90° + \phi$ with K_2. The second composition plane (H_1), which is perpendicular to η_1, is identified as the plane containing the rotation axis ⟨110⟩ and the vector k_1, which is perpendicular to the plane K_1 (Fig. 1).

Rotation of a BCC crystal about a ⟨110⟩ axis generally occurs during dislocation glide in $<\bar{1}1\bar{1}>$ directions in $\{\bar{1}12\}$ slip planes, and this is

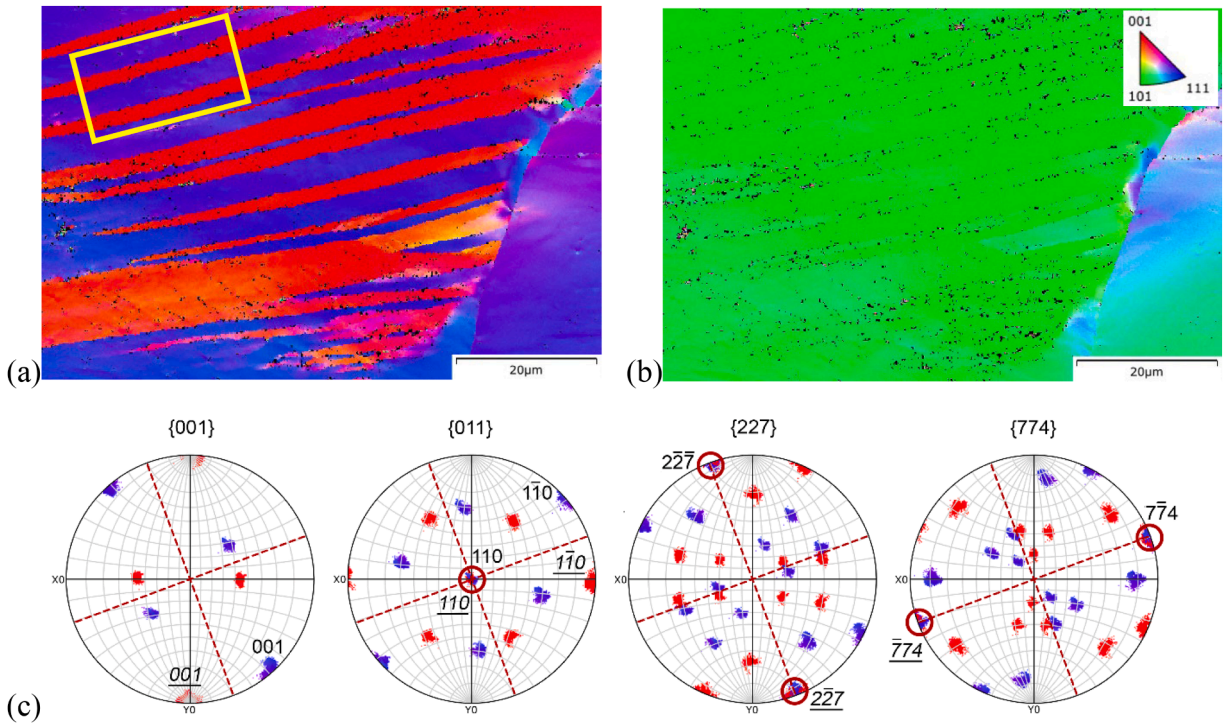

Fig. 11. A HfNbTaTiZr sample after deformation at 600 °C: (a,b) IPF maps of twins and the parent grain orientations in (a) Y (vertical) and (b) Z (normal) directions. The twins are not seen on the Z IPF map indicating that both the grain and the twins have the same orientation in Z direction. (c) Scattered-orientation pole figures from the region outlined in (a). The common poles are circled. The poles from the twins are red and their indexes are underlined, and the poles from the parent grain are blue. The twins' poles are rotated 44° clockwise about the common [110] pole relative to the respective poles from the matrix grain. Two orthogonal dashed lines crossing the centers of the stereographic projections represent the traces of the $(\bar{2}27)_M$ || $(2\bar{2}7)_T$ and $(7\bar{7}4)_M$ || $(7\bar{7}\bar{4})_T$ composition (mirror) planes. The twinning elements are: $P = (110)$, $K_2 = (\bar{1}10)$, $\eta_2 = [00\bar{1}]$, $K_1 = (2\bar{2}\bar{7})$, $\eta_1 = [\bar{7}7\bar{4}]$, $2\phi = 44.0°$ and $s = 0.808$.

Table 2
Deformation twins identified in HfNbTaTiZr after compression deformation at 23 °C, 400 °C and 600 °C.

T, °C	K_1	η_1	K_2	η_2	P	2ϕ (°)	s
23	$(1\bar{8}1)$	[414]	$(\bar{1}0\bar{1})$	[010]	$(\bar{1}01)$	20.05	0.354
23	$(1\bar{6}1)$	[313]	$(\bar{1}0\bar{1})$	[010]	$(\bar{1}01)$	26.53	0.471
23	$(5\bar{1}1)$	$[\bar{2}\bar{5}5]$	$(01\bar{1})$	[100]	(011)	31.58	0.566
400	$(1\bar{7}1)$	[727]	$(\bar{1}0\bar{1})$	$[0\bar{1}0]$	$(10\bar{1})$	22.84	0.404
400	(151)	$[5\bar{2}5]$	$(\bar{1}0\bar{1})$	$[0\bar{1}0]$	$(10\bar{1})$	31.58	0.566
600	$(2\bar{2}\bar{7})$	$[\bar{7}7\bar{4}]$	$(\bar{1}10)$	$[00\bar{1}]$	(110)	44.0	0.808

one of the widely accepted mechanisms of formation of deformation kinks (see Fig. 2 and the related text). However, crystallographic analyses of the reported features allowed us to confirm that these are deformation twins rather than kinks. Indeed, a deformation kink forming by rotation about ⟨110⟩ should have $K_2 = \{\bar{1}12\}$ and $\eta_2 = <\bar{1}1\bar{1}>$, which, during kinking, rotate to the positions K_2' and η_2', respectively, and the rotation angle 2ϕ generally increases with increasing the plastic deformation inside the kink band [20,32–34]. Additionally, K_2 and K_2', as well as η_2 and η_2', should have a reflection (mirror) symmetry across the kink boundary K_1. In other words, the direction η_1, which is normal to the rotation axis ⟨110⟩ and lays in plane K_1, should have the same angle ϕ with $K_2 = \{\bar{1}12\}_M$ and $K_2' = \{\bar{1}12\}_{KB}$. (The subscript 'KB' indicates that the respective plane belongs to the kink band). None of these agrees with the experiment. In particular, none of the planes, which are parallel to the rotation axis ⟨110⟩ and laying between $K_2 = \{\bar{1}12\}_M$ and $K_2' = \{\bar{1}12\}_{KB}$ provides a reflection symmetry between the rotated band and the parent grain. Instead, all the bands reported here have $K_2 = \{1\bar{1}0\}$ and $\eta_2 = \langle 001\rangle$, they all have a reflection symmetry with the parent grain across the band boundary K_1 and two-fold rotation symmetry about the direction η_1 and thus these bands follow twin laws and they should be considered as deformation twins. That is, in these deformation twins K_1 has the same angular distance 90°- ϕ with $K_2 = \{1\bar{1}0\}_M$ and $K_2' = \{1\bar{1}0\}_T$, which have the angular distance 2ϕ. The observed small variations in 2ϕ for the same twin can be explained by the accumulation of dislocations near twin boundaries during continuous deformation of the parent grain and the twin after the twin formation at earlier stages of deformation.

It is worth noting that the crystallographic analysis of the observed deformation twins in the Senkov alloy indicates that they can be interpreted as rotation twins rather than shear twins by expanding the current definition of rotation twins. The difference between the shear and rotation twins was discussed by Cahn [35] and the current definition of rotation twins was first given by Barrett and Massalski [36] (p. 406): "Crystals are rotation twins if a two-, three-, four- or six-fold rotation about a twinning axis produces the orientation of the other. The rotation axis lies either in the twinning plane or normal to it and is not a symmetry element of the individual crystals." The fundamental difference between the shear and rotational twins lies in the formation mechanism. Rotational twins involve a rotation of crystal domains, while shear twins involve shearing or sliding of crystal planes. Thus, rotational twins are characterized by a rotation axis and angle, while shear twins are characterized by a shear plane and direction. A typical example of a rotation twin in a cubic crystal is a twin formed by 60° rotation about ⟨111⟩ axis. In a simple cubic metal this twin is crystallographically similar to a shear twin $<\bar{1}\bar{1}1>\{112\}$; however, this is not the case in alloys having complex ordered cubic structures.

Our crystallographic analysis shows that formation of rotational twins in cubic crystals is not limited by a 180°, 120°, 90° or 60° rotation about the twinning axis. In particular, a much larger number of discrete rotation angles about a ⟨110⟩ axis can produce twin orientations. Indeed, the ⟨110⟩ zone in a cubic crystal contains two planes of

Table 3
Some rotational twins and twinning elements predicted from the current analysis, beyond the experimentally identified cases shown in Table 2.

Rotational axis	Rotational angle, 2ϕ (°)	K_1	η_1	K_2	η_2
<110>	17.89	{1$\bar{1}$9}	<$\bar{9}$92>	{$\bar{1}$10}	<001>
<110>	22.84	{1$\bar{1}$7}	<$\bar{7}$72>	{$\bar{1}$10}	<001>
<110>	38.94	{1$\bar{1}$4}	<$\bar{2}$21>	{$\bar{1}$10}	<001>
<110>	50.4	{1$\bar{1}$3}	<$\bar{3}$32>	{$\bar{1}$10}	<001>
<110>	34.89	{2$\bar{2}$9}	<$\bar{9}$94>	{$\bar{1}$10}	<001>
<110>	58.99	{2$\bar{2}$5}	<$\bar{5}$54>	{$\bar{1}$10}	<001>
<110>	55.88	{3$\bar{3}$8}	<$\bar{4}$43>	{$\bar{1}$10}	<001>
<100>	12.68	{0$\bar{1}$9}	<091>	{010}	<001>
<100>	14.25	{0$\bar{1}$8}	<081>	{010}	<001>
<100>	16.26	{0$\bar{1}$7}	<071>	{010}	<001>
<100>	18.92	{0$\bar{1}$6}	<061>	{010}	<001>
<100>	22.62	{0$\bar{1}$5}	<051>	{010}	<001>
<100>	28.07	{0$\bar{1}$4}	<041>	{010}	<001>
<100>	36.87	{0$\bar{1}$3}	<031>	{010}	<001>

symmetry, {001} and {1$\bar{1}$0}. Accordingly, the crystallographic direction <$u\ \bar{u}\ \bar{w}$> is a reflection of the direction <$u\ \bar{u}\ w$> in the plane {1$\bar{1}$0} and the direction <$w\ \bar{w}\ 2u$>, which is perpendicular to ⟨110⟩ and <$u\ \bar{u}\ \bar{w}$>, is a reflection of the direction < $\bar{w}\ w\ 2u$> in the plane {001}. These four crystallographic directions, <$u\ \bar{u}\ \bar{w}$>, <$u\ \bar{u}\ w$>, <$w\ \bar{w}\ 2u$> and <$\bar{w}\ w\ 2u$>, as well as normals ⟨001⟩ and <1$\bar{1}$0> to the respective {001} and {1$\bar{1}$0} planes, are all perpendicular to ⟨110⟩. Moreover, the angular distance ϕ between <$u\ \bar{u}\ \bar{w}$> and <1$\bar{1}$0>, <$u\ \bar{u}\ w$> and <1$\bar{1}$0>, <$\bar{w}\ w\ 2u$> and ⟨001⟩, and <$w\ \bar{w}\ 2u$> and ⟨001⟩ is the same and is given by Eq. (6):

$$2\phi_{<110>} = arcos\left[\left(2u^2 - w^2\right) / \left(2u^2 + w^2\right)\right] \quad (6)$$

Therefore, counterclockwise rotation about ⟨110⟩ of one part of the crystal relative to the other (matrix) part by the angle 2ϕ produces a twin pair with $\eta_2 = \langle 001\rangle$, $K_2 = \{1\bar{1}0\}$, $\eta_1 = <u\ \bar{u}\ \bar{w}>_M \,||\, <u\ \bar{u}\ w>_T$ and $K_1 = \{w\ \bar{w}\ 2u\}_M \,||\, \{\bar{w}\ w\ 2u\}_T$. In this configuration, $(u\ \bar{u}\ \bar{w})_M \,||\, (u\ \bar{u}\ w)_T$ and $(w\ \bar{w}\ 2u)_M \,||\, (\bar{w}\ w\ 2u)_T$ become mirror (composition) planes.

Using a similar approach, one can show that rotational twins can also be produced by rotation about the ⟨100⟩ axis to a fixed 2ϕ angle given by Eq. (7):

$$2\phi_{<100>} = arcos\left[\left(v^2 - w^2\right) / \left(v^2 + w^2\right)\right] \quad (7)$$

Here v and w are integers. The twinning elements for these rotational twins are:

$\eta_2 = \langle 001\rangle$, $K_2 = \{010\}$, $\eta_1 = <0\ v\ w>_M$ // $<0\ v\ \bar{w}>_T$ and $K_1 = \{0\ \bar{w}\ v\}_M$ // $\{0\ w\ v\}_T$.

A few twin configurations predicted from this analysis, as well as their twinning elements, are given in Table 3. The experimentally determined twins, given in Table 2, also follow the above-described rules of rotation about a ⟨011⟩ axis. Simulated stereographic projections of a few rotational twins identified in this work can be found in Section 3 of Supplementary Materials.

It should be noted that these rotational twins are equivalent to the shear twins having the same twinning elements only for crystals with a simple cubic structure. In the case of a complex cubic structure these modes of twinning can become different as twins produced by shear require extensive atom shuffling inside the cubic cells (sphere to ellipse transformation during simple shear, Fig. 1, may result in different relative locations of atoms inside the cell), while rotational twins do not require atom shuffling (no relative displacements of atoms occur inside the rotated crystal).

6. Summary and conclusion

Numerous deformation twins have been observed in a HfNbTaTiZr refractory high entropy alloy after compression deformation at room temperature, 400 °C and 600 °C. All these twins have been identified as rotational twins, which were formed by rotation of the parent grain about a ⟨110⟩ axis by 20.05°, 22.84. 26.53°, 31.58° or 44.0° This is the first report of these types of rotational deformation twins. Transformation matrices describing orientation relationships between the parent grain and the twins, and the twin composition planes were also reported.

The conditions required to form twin configurations in cubic crystals by the crystal rotation about ⟨110⟩ or ⟨100⟩ axes have been determined and a few rotational twins and the respective twinning elements have been identified. For the simple cubic crystals, these rotational twins are equivalent to the shear twins having the same twinning elements. However, in the case of a complex, ordered cubic structure these modes of twinning can become different, as twins produced by shear require extensive atom shuffling inside the cubic cells to hold mirror symmetry, while rotational twins do not require atom shuffling.

CRediT authorship contribution statement

Oleg N. Senkov: Writing – review & editing, Writing – original draft, Validation, Project administration, Investigation, Formal analysis, Data curation, Conceptualization. **Frederick Meisenkothen:** Writing – review & editing, Validation, Investigation, Formal analysis. **Robert Wheeler:** Writing – review & editing, Validation, Formal analysis.

Declaration of competing interest

The authors declare that they have no known competing financial interests or personal relationships that could have appeared to influence the work reported in this paper.

Acknowledgements

Work by O.N. Senkov and R. Wheeler was funded by the Metallic Materials and Processing Program at the Air Force Research Laboratory through the on-site contracts FA8650–21-d-5270 and FA8650–18-C-5291 managed, respectively, by MRL Materials Resources LLC, Xenia, OH, USA and UES, Inc., Dayton, OH, USA. Numerous discussions with Drs. S. Kuhr, B. McArthur and T. Butler are greatly appreciated.

Supplementary materials

Supplementary material associated with this article can be found, in the online version, at doi:10.1016/j.actamat.2024.120435.

References

[1] E.P. George, W.A. Curtin, C.C. Tasan, High entropy alloys: A focused review of mechanical properties and deformation mechanisms, Acta Mater. 188 (2020) 435–474.
[2] O.N. Senkov, J.M. Scott, S.V. Senkova, D.B. Miracle, C.F. Woodward, Microstructure and room temperature properties of a high-entropy TaNbHfZrTi alloy, J. Alloys Cmpds 509 (2011) 6043–6048.
[3] O.N. Senkov, J.M. Scott, S.V. Senkova, F. Meisenkothen, D.B. Miracle, C. F. Woodward, Microstructure and elevated temperature properties of a refractory TaNbHfZrTi alloy, J. Mater. Sci. 47 (9) (2012) 4062–4074.
[4] O.N. Senkov, S.L. Semiatin, Microstructure and properties of a refractory high-entropy alloy after cold working, J. Alloys Compounds 649 (2015) 1110–1123.
[5] O.N. Senkov, A.L. Pilchak, S.L. Semiatin, Effect of cold deformation and annealing on the microstructure and tensile properties of a HfNbTaTiZr refractory high entropy alloy, Metall. Mater. Trans. A 49A (2018) 2876–2892.
[6] M.L. Hu, W.D. Song, D.B. Duan, Y. Wu, Dynamic behavior and microstructure characterization of TaNbHfZrTi high-entropy alloy at a wide range of strain rates and temperatures, Int. J. Mech. Sci. 182 (2020) 105738.
[7] S. Zherebtsov, N. Yurchenko, D. Shaysultanov, M. Tikhonovsky, G. Salishchev, N. Stepanov, Microstructure and Mechanical Properties Evolution in HfNbTaTiZr Refractory High-Entropy Alloy During Cold Rolling, Adv. Eng. Mat. 22 (10) (2020) 105.
[8] Y.C. Huang, Y.C. Lai, Y.H. Lin, S.K. Wu, A study on the severely cold-rolled and annealed quaternary equiatomic derivatives from quinary HfNbTaTiZr refractory high entropy alloy, J. Alloys. Compd. 855 (2021).

[9] M.A. Charpagne, J.C. Stinville, F. Wang, N. Philips, T.M. Pollock, Orientation dependent plastic localization in the refractory high entropy alloy HfNbTaTiZr at room temperature, Mater. Sci. Eng. A 848 (2022).
[10] L.H. Mills, M.G. Emigh, C.H. Frey, N.R. Philips, S.P. Murray, J. Shin, D.S. Gianola, T.M. Pollock, Temperature-dependent tensile behavior of the HfNbTaTiZr multi-principal element alloy, Acta Mater. 245 (2023).
[11] X.J. Fan, R.T. Qu, Z.F. Zhang, Remarkably high fracture toughness of HfNbTaTiZr refractory high-entropy alloy, Journal of Materials Science and Technology 123 (2022) 70–77.
[12] C.C. Juan, M.H. Tsai, C.W. Tsai, W.L. Hsu, C.M. Lin, S.K. Chen, S.J. Lin, J.W. Yeh, Simultaneously increasing the strength and ductility of a refractory high-entropy alloy via grain refining, Mater. Lett. 184 (2016) 200–203.
[13] S. Chen, K.K. Tseng, Y. Tong, W. Li, C.W. Tsai, J.W. Yeh, P.K. Liaw, Grain growth and Hall-Petch relationship in a refractory HfNbTaTiZr high entropy alloy, J. Alloys Compounds 795 (5) (2019) 19–26.
[14] J.P. Couzinie, L. Lilensten, Y. Champion, G. Dirras, L. Perriere, I. Guillot, On the room temperature deformation mechanisms of a TiZrHfNbTa refractory high-entropy alloy, Mater. Sci. Eng. A 645 (2015) 255–263.
[15] S.I. Rao, C. Woodward, B. Akdim, O.N. Senkov, D. Miracle, Theory of solid solution strengthening of BCC chemically complex alloys, Acta Mater. 209 (2021) 116758.
[16] G. Dirras, L. Lilensten, P. Djemia, M. Laurent-Brocq, D. Tingaud, J.P. Couzinie, L. Perriere, T. Chauveau, I. Guillot, Elastic and plastic properties of as-cast equimolar TiHfZrTaNb high-entropy alloy, Mater. Sci. Eng. A 654 (2016) 30–38.
[17] L. Lilensten, J.P. Couzinie, L. Perriere, A. Hocini, C. Keller, G. Dirras, I. Guillot, Study of a bcc multi-principal element alloy: Tensile and simple shear properties and underlying deformation mechanisms, Acta Mater. 142 (2018) 131–141.
[18] J. Cizek, P. Hausild, M. Cieslar, O. Melikhova, T. Vlasak, M. Janecek, R. Kral, P. Harcuba, F. Lukac, J. Zyka, J. Malek, J. Moon, H.S. Kim, Strength enhancement of high entropy alloy HfNbTaTiZr by severe plastic deformation, J. Alloys. Compd. 768 (2018) 924–937.
[19] S. Wang, M. Wu, D. Shu, G. Zhu, D. Wang, B. Sun, Mechanical instability and tensile properties of TiZrHfNbTa high entropy alloy at cryogenic temperatures, Acta Mater. 201 (2020) 517–527.
[20] A.G. Crocker, J.S. Abell, The crystallography of deformation kinking, Philosophical Magazine 33 (2) (1976) 305–310.
[21] E.O. Hall, Twinning and Diffusionless Transformations in Metals, Butterworths Publications, London, UK, 1954.
[22] B.A. Bilby, A.G. Crocker, The theory of crystallography of deformation twinning, Proc. Royal Soc. (London), Series A, Mathematical and Physical Sciences 288 (1413) (1965) 240–255.
[23] J.W. Christian, S. Mahajan, Deformation Twinning, Progr. Mater. Sci. 39 (1995) 1–157.
[24] D. Zhang, L. Jiang, B. Zheng, J.M. Schoenung, S. Mahajan, E.J. Lavernia, I. J. Beyerlein, Deformation Twinning (Update), Reference Module in Materials Science and Materials Engineering (2016) 1–24.
[25] A. Ostapovets, A. Serra, Review of non-classical features of deformation twinning in hcp metals and their description by disconnection mechanisms, Metals. (Basel) 10 (2020) 1134.
[26] J.P. Hirth, J. Wang, Extension of the classical theory for types I and II twinning, J. Mater. Res. 36 (2021) 2615–2622.
[27] Y. Gao, Y. Zhang, Y. Wang, Determination of twinning path from broken symmetry: A revisit to deformation twinning in bcc metals, Acta Mater. 196 (2020) 280–294.
[28] E. Goo, T. Duerig, K. Melton, R. Sinclair, Mechanical twinning in $Ti_{50}Ni_{47}Fe_3$ and $Ti_{49}Ni_{51}$ alloys, Acta Metall 33 (9) (1985) 1725–1733.
[29] R.C. Pond, J.P. Hirth, Topological model of type II deformation twinning, Acta Mater. 151 (2018) 229–242.
[30] M. Bevis, A.G. Crocker, Twinning modes in lattices, Proc. Royal Soc. Lond. A 313 (1969) 509–529.
[31] R.W.K. Honeycombe, The Plastic Deformation of Metals, 2nd Ed., Edward Arnold, London, UK, 1984.
[32] Y. Yang, S.Q. Wu, G.P. Li, Y.L. Li, Y.F. Lu, K. Yang, P. Ge, Evolution of deformation mechanisms of Ti-22.4Nb-0.73Ta-2Zr-1.34O alloy during straining, Acta Mater. 58 (2010) 2778–2787.
[33] N.Y. Yurchenko, E.S. Panina, S.V. Zherebtsov, M.A. Tikhonovsky, G.A. Salishchev, N.D. Stepanov, Microstructure evolution of a novel low-density TiCrNbV refractory high entropy alloy during cold rolling and subsequent annealing, Mater. Charact. 158 (2019).
[34] S. Wang, M. Wu, D. Shu, B. Sun, Kinking in a refractory TiZrHfNb0.7 medium-entropy alloy, Mater. Lett. 264 (2020).
[35] R.W. Cahn, Twinned crystals, Adv. in Phys. Quart. Suppl. Phyl. Mag. 3 (1954) 363–445.
[36] C.S. Barrett, T.B. Massalski, The Structure of Metals, 3rd ed., McGraw-Hill, New York, 1966.